Electrochemical study of carbon dioxide reduction at copper-palladium nanoparticles: Influence of the bimetallic composition in the CO poisoning tolerance

E. Torralba, N. Blanchard, C. Cachet-Vivier, D. Muller-Bouvet, J. González, S. Bastide

Electrochemical study of carbon dioxide reduction at copper - palladium nanoparticles: influence of the bimetallic composition in the CO poisoning tolerance.

E. Torralba [1]*, N. Blanchard [1], C. Cachet-Vivier [1], D. Muller-Bouvet [1], J. González [2], S. Bastide [1]

[1] *Institut de Chimie et des Matériaux Paris-Est, Université Paris-Est, UMR 7182 CNRS—UPEC, 2 rue H. Dunant, 94320 Thiais, France*

[2] *Departamento de Química Física, Facultad de Química, Regional Campus of International Excellence "Campus Mare Nostrum",Universidad de Murcia, 30100 Murcia, Spain*

*Corrresponding author: torralba-penalver@icmpe.cnrs.fr

Keywords: cavity microelectrode, solid solution nanoalloy, cyclic voltammetry, chronoamperometry, CO stripping

Abstract

A study of the CO_2 electrochemical reduction reaction (CO_2RR) at $Pd_{100-x}Cu_x$ solid solution type nanoalloys is presented. Cyclic voltammetry and chronoamperometry are used in combination with a cavity microelectrode (CME) for the first time.

Low-distorted voltammetric signals obtained with the CME evidence that for alloys with low or moderate Cu content (up to 50 at.%) the typical CO_2RR inhibition peak, related to

CO blocking Pd active sites, becomes a current plateau. Interestingly, the plateau height matches the theoretical value corresponding to the steady state current of a microdisc. This fact indicates a better tolerance of $Pd_{100-x}Cu_x$ towards CO poisoning and also the attainment of a pseudo-steady state where mass transport should be controlled by diffusion. The synergy between Cu and Pd is thus established for the first time at the level of the voltammograms.

The chronoamperometric responses exhibit three well defined regions corresponding to 1) double layer charging and diffusion/reaction establishment, 2) beginning of CO poisoning by formation of a CO adlayer and (3) final collapse of the catalytic activity at a critical time, t_c, which depends directly on the bimetallic composition. A plot of t_c *vs.* Pd content exhibits a clear volcano shape, from which ~ $Pd_{72}Cu_{28}$ is identified as a close to optimal composition in terms of CO tolerance and $Pd_{35}Cu_{65}$ as the composition from which the advantage of alloying Pd with Cu is lost.

An in-depth analysis of the I/V response and its evolution with composition and time is performed in the CO_2RR and CO stripping regions. As a result, the possibility of developing a method to further increase the catalyst lifetime based on periodical releasing of “CO-like” intermediates by CO stripping is proposed.

1. Introduction

Carbon dioxide (CO_2) is a greenhouse gas that produces global warming, with undesirable climate effects. Hence, controlling the CO_2 atmospheric levels is a research priority. Among the possible technologies to sustainably transform CO_2, electrochemical CO_2 Reduction Reaction (CO_2RR) to useful low-carbon fuels or chemicals (CO, CH_4, CH_3OH, HCOOH,…) is particularly attractive due to unique merits: operation under mild conditions, wide product window, applicability in industrial processes and full compatibility with renewable energy sources [1]. Despite many advances, the electrochemical CO_2 conversion process remains still challenging, without large scale implementation so far. The main persisting drawbacks are (i) the high overpotential required (C=O bond energy of 803 kJ/mol), (ii) the formation of a mixture of products implying costly separation steps, (iii) the moderate yields in hydrocarbons (e.g. up to 40 % for CH_4 with state of the art Cu-based catalyst [2]) and (iv) the low solubility of CO_2 in water at RT (0.03 mol L^{-1}). Concomitant hydrogen evolution (HER) and CO surface poisoning are other important issues. In addition, the current knowledge of the reaction mechanisms is limited, which hinders faster developments in the field [2].

Metal catalysts in various forms have been tested for CO_2RR, bulk or nanostructured, monometallic or, more recently, bimetallics [3]. Nanostructured metals (e.g. nanoparticles (NPs), nanoporous structures) have higher catalytic activities due to a greater number of active sites (e.g. the intrinsic catalytic activity of nanoparticulate Ag is 20 times higher than that of bulk Ag) [4]. Catalytic activity, efficiency and selectivity can be boosted by using nanostructured bimetallics. The introduction of a second metal increases the variety of structural patterns and the chemical heterogeneity of the surface (geometrical effect) and also modifies the energy levels of the main metal (electronic effect), as a function of the

composition and structure of the bimetallic. This impacts the selectivity and faradic efficiency by changing the degree of stabilization of the adsorbed intermediates (CO*, H*, HCOH*) [3].

In this work, we report on the synthesis and characterization of CuPd NPs with different compositions and their application as nanoelectrocatalysts for CO_2RR. Some studies on CuPd under different configurations (*e.g.* Cu overlayers on Pd [5,6], Pd-decorated Cu electrodes [7], mesoporous CuPd films [8], CuPd NPs of different mixing patterns and morphologies [9–13]) have pointed out its better performances with respect to Pd and Cu taken separately in terms of current density, stability and selectivity. These works have shown, for example, that a moderate fraction of Cu atoms in the Pd structure (always lower than 50 at.%, more frequently around 15-25% at.%) can improve the resistance to CO-poisoning of Pd while keeping its low overpotential for CO and HCOOH production [5,10,13,14]. Also, tailoring the bimetallic structure and morphology can help to tune the product distribution towards hydrocarbons [11,12], alcohols [6], syngas [9,13] or formic acid [5,14].

In the majority of the aforementioned works, electrochemistry has been used as a mere tool for product generation (i.e. quantitative electrolysis at selected potentials for faradaic efficiency determinations) and low attention has been paid to record and interpret the electrochemical signals. More in-depth electrochemical studies could help increasing the understanding of CO_2 reduction on $Pd_{100-x}Cu_x$ compounds and establishing additional links between physico-chemical data (from XPS, Raman, TPD-CO, etc) and theoretical calculations (DFT). Finally, in the studies dealing with $Pd_{100-x}Cu_x$ NPs no attention has been payed to the elemental arrangement of the bimetallics (phase separated, intermetallic or solid solutions), with some noticeable exceptions [11]. Systematic studies with well-defined bimetallic structures are lacking.

Following this trend of thought, we have carried out in this work an in-depth electrochemical study of the CO_2RR at $Pd_{100-x}Cu_x$, paying special attention to the influence of the bimetallic composition on the voltammetric response and on the related CO-poisoning. Solid solutions in the form of NPs have been chosen as most typical and easy to synthetize bimetallic alloys. The experiments have been carried out using a Cavity Microelectrode (CME). This electrode allows fast characterization of powder materials, avoids addition of external reagents (*i.e.* binders, carbon) and provides I/V responses with very low distortion [15]. These properties make the CME a useful tool to gain insights into the mechanisms followed by key steps of electrochemical processes, in this case CO_2RR. As a result, the synergy between Cu and Pd, already observed by other methods (such as TPD-CO or XPS [5]), is clearly established at the electrochemical level.

2. Experimental

2.1 Synthesis of catalysts

Pd, Cu and $Pd_{100-x}Cu_x$ nanoparticles, with targeted *x* values equal to 25, 50, 75 and 85, were synthetized by a soft chemical route in aqueous media, using $Pd(NO_3)_2$ and $Cu(SO_4)$ metal salts as precursors and $NaBH_4$ as reducing agent (from Alfa Aesar, Acros Organics and Prolabo, respectively). First, the appropriate quantities of metal precursors (*e.g.* 1 mmol of $CuSO_4$ and 1 mmol $Pd(NO_3)_2$ for $Pd_{50}Cu_{50}$) are dissolved in 150 mL of 0.05 mol L^{-1} H_2SO_4 (pH = 1) at ~ 0°C (ice bath) and degassed with argon for 30 minutes under constant stirring. Second, 50 mL of 4 10^{-3} mol L^{-1} $NaBH_4$ (at ~ 0°C) are poured at once in the metal precursors solution under vigorous stirring. Its colour changes instantaneously from light brown to black and a powder suspension appears. Stirring is maintained for one hour (under argon at 0°C) to ensure completion of the reaction.

The obtained powder is collected by centrifugation/decantation and washed 5 times with ultra-pure water and 5 times with absolute ethanol. The precipitate is then sonicated with the minimum quantity of ethanol (*c.a.* 150 - 200 µL) during 5 min to avoid powder agglomeration and left to dry under primary vacuum. Before use, as-synthetized bimetallic powders were stored under vacuum. Pure Cu and Pd NPs were synthesized in the same way. Material yields were above 90 % weight in all cases.

2.2 Physical Characterization

Structural characterization was performed by X-Ray diffraction (XRD) using a D8 advanced Bruker diffractometer (copper K_α radiation). The software EVA was used for XRD data processing. CellRef and EVA were used to obtain initial values of the lattice parameter and the crystallite size (Scherrer equation), respectively. Optimized values were calculated by Rieldvelt refinement.

Morphology and composition (elemental analysis) were analyzed by Scanning Electron Microscopy (SEM) coupled to Energy Dispersive X-ray Analysis (SEM-EDX) with a FEG microscope from Zeiss. The average NP size was determined using the software ImageJ.

2.3 Electrochemical measurements

A three-electrode cell (50 mL) was used to carry out electrochemical measurements with an Autolab PGSTAT 30 potentiostat from Metrohm equipped with the software NOVA.

The working electrode was a homemade cavity microelectrode (CME) consisting of a platinum wire embedded in a glass rod with at the tip a cavity of 25 µm in diameter and 22 µm in depth (the bottom of the cavity corresponding to the end of the platinum wire). The cavity has a surface opening of 4.9 10^{-6} cm^2 and a volume of ~ 10^{-7} cm^3. The CME is filled with the powder material by simple mechanical pressure of the electrode tip against the powder. It is emptied by sonication in HNO_3 (65%)/water (1:1) for 1-2 min and refilled with new $Pd_{100-x}Cu_x$ powder for each electrochemical test. Fabrication and use of CMEs are described in reference [16].

A Pt wire was used as counter electrode and an Ag/AgCl electrode as reference (E = 0.209 V *vs.* NHE). All potentials were converted to the RHE reference scale unless otherwise noted (E *vs.* RHE = E *vs.* Ag/AgCl + 0.209 + 0.059 pH).

The electrocatalytic reduction of CO_2 was conducted in 0.1 mol L^{-1} $NaHCO_3$ at room temperature (pH = 8.4). Before each experiment, 30 mL of electrolyte were purged with Ar for 10 min and the electrocatalyst surface was subjected to the electrochemical pre-treatment explained in section 3.2 of results and discussion. The electrolyte was then bubbled with CO_2 (Alphagaz N45) for 20 min to ensure CO_2 saturation (pH ~ 6.55, [CO_2] = 33 mmol L^{-1}). A CO_2 atmosphere was maintained throughout the experiment. Current densities correspond to the measured current divided by the cavity opening area (i.e. 4.9

10^{-6} cm^2), under the assumption that a CME densely filled with a metal powder behaves like a microdisk, as exemplified in Figure S1 of the supporting information (SI).

3. Results and discussion

3.1 Composition and structural characterization

The morphology and elemental composition of the synthesized nanopowders have been examined by SEM-EDX. SEM images at different magnifications are given in Figure 1. They revealed homogeneously distributed spherical NPs, with average sizes of ~ 70 nm for Cu, ~ 26 nm for Pd and ~ 10 - 12 nm for the bimetallics (Table 1). EDX analysis revealed no particular domain of pure Cu or Pd, which suggests that the samples are solid solutions type alloys. The obtained compositions are closed to the targeted ones (see Table 1).

<Figure 1>

Figure 2A shows the XRD patterns of the mono and bimetallic nanopowders. All samples display the characteristic diffraction peaks of a cubic face centered structure (space group Fm-3m, as for pure Pd and Cu [17,18]). The XRD peaks corresponding to the bimetallics are wider than those of pure metals, which indicates smaller crystallite size for the $Pd_{100-x}Cu_x$ nanoalloys. The crystallite size were evaluated from Rietveld refinement of each XRD patterns (Table 1). It decreases steadily from 7 nm for pure Pd to 3 nm for $Pd_{55}Cu_{45}$ and then increases to 22 nm for pure Cu. Hence, alloying of Cu and Pd reduces the mean crystallite size and thus promotes the formation of nanoscale structures, which can be very interesting for electrocatalysis applications.

<Table 1>

A progressive shift of the diffraction peaks (111, 002, 022, 113, 222) as the Cu fraction *x* increases is observed. Lattice parameters have been obtained by Rietveld refinement of the

diffractograms. Figure 2B gives a plot of the refined lattice parameters as a function of the Pd content (at.% of Pd determined by EDX, see Table1). According to Vegard's law [19], the unit cell parameters of ideal and continuous substitutional solid solutions, in which atoms substitute each other randomly, should vary linearly with the composition. The lattice parameter of the Cu–Pd nanoalloys exhibits a positive deviation from Vegard's law. This deviation may result from non-ideality of the solid solution enthalpy of mixing and weaker Cu–Pd interactions compared to pure Cu–Cu and Pd–Pd, as already reported by Subramanian and Laughlin [20] and Allemand et al. [21]. In the case of $Pd_{55}Cu_{45}$ for which the deviation with Vegard's law is more important, the disagreement could be explained by the presence of a mixture of two phases (rather than a single phase) too close in composition to be resolved (under the conditions of this study).

<Figure 2>

3.2 Electrochemical study of CO_2RR on $Pd_{100-x}Cu_x$

3.2.1 Electrochemical pre-treatment

The electrochemical pre-treatment (in 0.1 mol L^{-1} $NaHCO_3$, pH = 8.4) under argon consisted in: (1) two CVs from OCP to -0.8 V *vs.* RHE (-1.5 V *vs.* Ag/AgCl), to remove Pd and Cu native oxides; (2) a constant polarization at c.a. - 0.3 V *vs.* RHE (-1 V *vs.* Ag/AgCl) during 120 seconds to hydrogenate Pd sites, (3) two CVs from the new OCP to -0.8 V *vs.* RHE, to ensure a reproducible response. Figure S2 in the SI gives typical electrochemical responses obtained during this pre-treatment.

The main purpose of the pre-treatment is to supress the hydrogen sorption response of Pd sites in the voltammograms recorded with $Pd_{100-x}Cu_x$ and Pd. This allows obtaining CO_2RR responses which are easier to analyse and better suited to physical interpretation. To show the influence of the H-related responses in the CO_2RR curve, Figure 3 gives the CV

responses obtained under argon (A) and CO_2 (B) with a CME filled with Pd NPs when the electrochemical pre-treatment is applied (solid lines) and when it is not (dash-dotted lines).

<Figure 3>

The typical CV features of Pd are clearly recognisable in the CV under Ar of the non-pre-treated surface (dashed dotted line in Figure 3a). That is, starting from positive potentials: two cathodic peaks (C_{oxides}), centered at +0.45 V *vs.* RHE, corresponding to the reduction of native Pd oxides; one cathodic plateau (C_α), starting at +0.2 V *vs.* RHE, corresponding to the formation of a Pd hydride in its α phase (α-PdHx) and a cathodic peak C_β at -0.46 V *vs.* RHE, corresponding to the transition of α- to β-PdHx. On the anodic sweep, the anodic peak $A_{\alpha,\beta}$ at +0.65 V corresponds to hydrogen desorption from α,β-PdHx to Pd. More information about hydrogen sorption properties in Pd NPs studied with the CME can be found in [22]. Hence, if the CO_2RR is performed directly, the resulting CV is formed by three overlapped electrochemical signals (dash-dotted curve in Figure 3B) with only one corresponding to the CO_2RR process (C_1).

On the contrary, if the Pd surface is pre-treated, the resulting CV under Ar shows no traces of hydrogen sorption (solid line in Figure 3A). This indicates that Pd has been hydrogenated in its β phase (the potential of hydrogen desorption is not reached if the CV upper potential limit is below 0.2 V). The hydrogen related signals have been suppressed. If CO_2RR is performed on such pre-treated sample, the resulting CV exhibits only one, well defined peak for CO_2RR (C_1). These simpler electrochemical signals favour the physical interpretation of the associated phenomena (*e.g.*, how the alloy composition influences the rate limiting step of CO_2RR).

3.2.2 CV analysis of CO_2RR on $Pd_{100-x}Cu_x$

Figure 4 shows the CV responses of the different $Pd_{100-x}Cu_x$ nanopowders under CO_2 (red lines) and Argon atmosphere (black lines). Red and blue arrows indicate the main CO_2RR signals related to Cu and Pd sites, respectively.

<Figue 4>

When comparing the responses under Ar and under CO_2, all the nanoelectrocatalysts clearly exhibit a CO_2 reduction activity. CVs of pure metals show a well-defined peak located at -0.8 and -0.4 V *vs.* RHE for Cu (Figure 4A) and Pd (Figure 4D), respectively. These peaks have been attributed to the reduction of CO_2 to CO or "CO-like" intermediates (multibonded CO radicals, such as (HCOO), CHO, $C(OH)_2$ and CH_x [23–25]) that remain attached to the catalyst surface and inhibit the reaction. In the case of Cu, CO-like intermediates can be further reduced at more negative potentials to hydrocarbons and alcohols [25], but in the case of Pd they eventually lead to the deactivation of the surface (poisoning) [23,24]. The electrochemical features of Cu and Pd sites are also observed in $Pd_{100-x}Cu_x$ (see red and blue arrows in Figures 4B, C, D and F), but shifted to positive potentials values. This indicates that CO_2RR is thermodynamically favoured on bimetallics. In addition, their response is in general more intense than those of pure metals. The higher reduction currents and lower overpotentials point out that bimetallics have superior catalytic performances compared to pure metals, as developed in Figure 5.

Interestingly, when comparing CO_2RR on pure Pd (Figure 4D) and on bimetallics with low or intermediate Cu content (Figures 4C, E and F), a clear trend is observed: the peak for pure Pd (c.a. -0.4V *vs.* RHE) becomes a plateau as the concentration of Cu increases (especially for $Pd_{72}Cu_{28}$ and $Pd_{55}Cu_{45}$). Given that this peak is linked to the blocking of active Pd sites by CO, its transformation into a current plateau (*i.e.* controlled by mass transport in the electrolyte) clearly indicates a better tolerance of $Pd_{100-x}Cu_x$ to CO

poisoning. As far as we know, this is the first time that the cooperative effect between Cu and Pd is evidenced at the level of the CV responses.

The origin of this current plateau has been investigated by Tafel plots built from the voltammograms of Figure 4 (Figure S3 of the SI). In order to avoid mass transport influence, the current values selected were chosen at potentials corresponding to the foot of the wave. The Tafel slope values extracted for the bimetallics with low or intermediate Cu content were 135, 107, 124 and 142, mV dec^{-1} for Pd, $Pd_{87}Cu_{13}$, $Pd_{72}Cu_{28}$ and $Pd_{55}Cu_{45}$, respectively. These values suggest that CO and formate are the major reduction products under the experimental conditions of these experiments [26,27] and, more importantly, that the rate limiting step of the CO_2RR is an initial one-electron transfer (presumably to form a $CO_2^{\cdot -}$ anion radical that gets further adsorbed/reduced to generate the products [28]). For Cu and $Pd_{24}Cu_{76}$, the Tafel slopes reach 215 and 214 mV dec^{-1}, respectively, which could indicate a different rate limiting step or a reaction mechanism leading to a different product. For example, Tafel slopes as high as 175 mVdec^{-1} have been reported for methane formation on Cu [29].

In general, lower Tafel slopes are a sign of better electrocatalytic performances due to faster charge transfer kinetics. The results presented here thus evidence that $Pd_{100-x}Cu_x$ are favoured both thermodynamically (positive shift of the reduction potentials in CV) and kinetically (lower Tafel slopes), especially for $Pd_{87}Cu_{13}$ and $Pd_{72}Cu_{28}$.

Taking into account that the CME filled with metal NPs behaves like a microdisc (Figure S1 in the SI), a simple calculation of the theoretical current density plateau under steady state conditions, j_{ss}, for a single electron transfer based on Saito's equation [30] :

$$j_{ss} = - 4 n F D C / \pi r_0$$

gives a value of -68.1 mA cm^{-2} (with C_{CO2} = 33 mmol L^{-1}, $D_{CO2(water)}$ = 2.1 10^{-5} cm^2 s^{-1} [31] and r_0 = 12.5 10^{-4} cm). This value matches reasonably well the peak height obtained with

pure Pd (just before CO poisoning starts, *c.a.* -60.0 mA cm^{-2}) and the current density plateaus obtained for $Pd_{72}Cu_{28}$ and $Pd_{55}Cu_{45}$ (c.a. -68.0 and -77.0 mA cm^{-2}). This is consistent with the rate limiting step being an initial one electron transfer, and shows that, in the conditions of the experiment, CO_2RR at $Pd_{100-x}Cu_x$ reaches a pseudo steady-state where mass transport is controlled by diffusion.

The effect of the bimetallic composition on the current density and onset potential of the CO_2RR is depicted in Figure 5. In Figure 5A, the current density (absolute value) is plotted with respect to the Pd fraction at three potentials, each located in a specific product region according to the literature (HCOOH for E = -0.1V *vs.* RHE, CO for E = -0.4V and C2/C2+ for E ≤ 0.8V; see Table S1 in the SI). In Figure 5B, the onset potential and the overpotential required to reach an appreciable current density of 10 mA cm^{-2} have been plotted as a function of the Pd content.

<Figure 5>

As can be seen in Figure 5A, the current density follows a sort of Volcano plot with the Pd content. $Pd_{87}Cu_{13}$ is the composition providing the highest current density at -0.4 V *vs.* RHE, for which CO is usually the major product (see Table S1 in the SI). This is in agreement with recent studies pointing at $Pd_{85}Cu_{15}$ as the optimal composition for selective CO production [10]. The Volcano shape is less defined regarding low potentials (-0.1 V *vs.* RHE), typical of HCOOH production, for which $Pd_{55}Cu_{45}$, $Pd_{72}Cu_{28}$ and $Pd_{87}Cu_{13}$ deliver approximately the same current density. Regarding the CO_2RR onset potentials (Figure 5B), there is no appreciable difference between the different compositions. However, it is clear that $Pd_{100-x}Cu_x$ compounds with low or moderate content in Cu are desirable to reach significant current values (higher than 10 mA cm^{-2}).

3.2.3. Electrochemical stability of $Pd_{100-x}Cu_x$ nanoalloys for CO_2RR

The stability of $Pd_{100-x}Cu_x$ for CO_2RR has been evaluated by CV and CA experiments. Figure 6A shows the evolution of the current density with the cycle number at -0.5 V *vs.* RHE (*i.e.* just below the CO inhibition potential for pure Pd and in the plateau region for the bimetallics). Figures 6B - D give the complete CV signals for Cu, Pd and $Pd_{87}Cu_{13}$ (see Figure S4 of the SI for other compositions).

<Figure 6>

Several conclusions can be drawn from Figure 6. First, Cu retains its catalytic activity, with a stable current density upon cycling (see red diamonds line in Figure 6A and 6B), though with only moderate values at high overpotentials. Second, Pd gets quickly deactivated by CO poisoning (Figure 6C). Although Pd can provide appreciable current density values at relatively low overpotentials (*e.g.* 60 mA cm^{-2} at -0.5 V *vs.* RHE, first cycle in Figure 6A - black circles), more than 80% is already lost in the second cycle (*e.g.* 10 mA cm^{-2}, Figure 6A - black circles). On the contrary $Pd_{100-x}Cu_x$ surfaces have an intermediate stability between pure Cu and pure Pd, supporting 4-5 cycles before being deactivated (Figures 6A and 6D). The exception is $Pd_{24}Cu_{76}$, which gets partially deactivated after only one scan in CV and reaches a current density similar to that measured on Cu. $Pd_{72}Cu_{28}$ seems slightly more stable than the other compositions, as confirmed by the CA experiments presented below.

Figure 7A shows the CA responses for CO_2RR obtained with $Pd_{100-x}Cu_x$, Pd and Cu nanopowders at E = -0.4 V *vs.* RHE (solid lines), together with the theoretical response for a single one electron transfer at a microdisc (dash-dotted line) obtained from Shoup-Szabo's equation [30] (see S3 in the SI).

<Figure 7>

Three regions, determined by the different slopes of the *j/t* curves, can be identified in the CA responses. In the first region (for time values lower than 50 seconds) the current drops steeply, due to double layer charging and establishment of the initial diffusion/reaction regime. In the second region, at specific times values depending on the composition, the decrease in current is mitigated as a CO adlayer is progressively formed on Pd sites [14,27]. A third region, characterized by a sharp drop of the current down to zero, is observed for all samples. Similar *j*/*t* signals have been reported in two cases: CO_2RR with Pd NPs and with a nanoporous $Pd_{75}Cu_{25}$ alloy [14,27].

The experimental CA curves do not match the theoretical value of -68.1 $mAcm^{-2}$ corresponding to the attainment of the pseudo-steady state (reached by the theoretical CA curve at t = 0.2 s). Instead, they cross the j_{ss} value at times ranging from 5 to 30 s (depending on the composition) and continue decreasing. This behaviour may contrast the observations from CV in Figure 4 (theoretically j_{ss} should be identical for CV and CA for a simple process [30]). However, it simply shows that, in terms of temporal influence, the kinetics associated with the second stages of CO_2RR at $Pd_{100-x}Cu_x$ nanopowders (i.e. those leading to CO poisoning) become significant over time (and hence the experimental *j* does not fit with that of a simple electron transfer anymore). From a practical point of view, the observation is that in long-time electrolysis at this particular potential (-0.4 V *vs.* RHE) CO will inexorably poison the electrocatalytic surface, as consistently observed through cycling (Figure 6).

The specific physical phenomena behind the last and abrupt current drop is not clear, since a complex interplay between solution (e.g. mass transport, CO_2 reduction) and surface processes (CO blocking of Pd sites) is taking place. Nevertheless, it certainly indicates a complete collapse of the catalyst active surface due to total CO poisoning. It occurs at a critical time (hereafter referred to as t_c, chosen as the intersection of the median and final

slopes) highly dependent on the bimetallic composition. In Figure 7B, t_c is plotted *vs.* the Pd content. As can be seen, it clearly follows a volcano plot, pointing at $Pd_{72}Cu_{28}$ as the optimal composition in terms of CO poisoning resistance (highest t_c). As far as we know, this is the first time that this kind of plot is built for $Pd_{100-x}Cu_x$, and for CO_2RR at bimetallics in general. At the potential selected for the experiments, pure Pd gets fully poisoned after 400 s. However, if 28 % of the Pd atoms are replaced by Cu atoms, the critical time for surface poisoning is multiplied by a factor of 2.75 (t_c = 1100s), while intuitively t_c should decrease since there are fewer Pd sites. Similarly, Figure 7B reveals that a bimetallic with a Pd fraction as low as in $Pd_{35}Cu_{65}$ would not be poisoned faster than pure Pd (identical t_c values). This is a clear demonstration of the synergy between the two metals.

3.2.4. CO stripping

To provide a wider picture about the influence of the alloy composition on CO poisoning of $Pd_{100-x}Cu_x$ nanoelectrocatalyts, the potential range in the CV measurements was extended to the region of CO stripping. Figure 8 shows the 1st, 2nd and 9th cycle of a series of 10 consecutives cycles carried out with Pd (Figures 8A-C) and $Pd_{87}Cu_{13}$ (Figures 8D-F), under CO_2 (red lines) and argon (black lines). The most representative electrochemical features under CO_2 are identified by the letters C or A, as in Figure 3. An analogous figure for $Pd_{55}Cu_{45}$ is given in Figure S6 of the SI.

<Figure 8>

The 1st cycle for Pd under CO_2 is given in Figure 8A. Besides the electrochemical features already described in Figure 3 (*i.e.* C_1, C_{oxides} and $A_{\alpha,\beta}$), two anodic peaks appear, A_1 and A_1', at +1.05 V and +1.2 V *vs.* RHE. According to the literature, these peaks are due to CO stripping [24,27]. They are attributed to (i) “CO-like” intermediates (CO and multibonded

CO radicals) that desorb at different potentials [24] and (ii) two different Pd sites (terraces and edges) where CO is adsorbed weakly and strongly, respectively. This last hypothesis has been supported by DFT studies [27,32].

The second cycle (Figure 8B) differs by the appearance of the C_α and C_β signals corresponding respectively to the hydrogenation of Pd into α-PdH_x (at *c.a.* 0 V *vs.* RHE) and β-PdH_x (at *c.a.* -0.7 V). The latter does not lead to a well-defined peak under the conditions of this experiment (v = 20 mV s^{-1}, see also Figure 3), but can be identified by an increase of the current density at potentials at which C_1 is already under limiting current conditions (around -0.7 V *vs.* RHE). A global increase in the cathodic current density is observed during the second cycle with respect to the first, as a consequence of the recovering of H related signals when the potential is allowed to go in the anodic range.

In situ XAS studies of CO_2RR combined with DFT have shown that the transition from a mixed α+β hydride phase to the β-phase results in a change of the reaction product (HCOOH to CO). This is induced by an earlier change in reaction intermediates, from $HCOO_{ad}$ (precursor of HCOOH) to $COOH_{ad}$ (precursor of CO) [27,32]. This phase transition begins at *c.a.* -0.2 V *vs.* RHE (CO_2RR onset potential, see Figure 8B) and ends at *c.a.* -0.5 V *vs.* RHE (just after the CO inhibition peak in Figure 8B) [27,32]. This has been attributed to variations in adsorption strength of the reactants (CO_2, H), intermediates (CO, HCOOad, COOHad) and products, and to the thermodynamic and kinetic properties of the two phases as well.

On account of the competition between CO_2RR and H at active catalytic sites, the H-related signals (C_α, C_β, $A_{\alpha,\beta}$ and HER) decrease progressively with the number of CV cycles [23,24]. In Figure 8C, the peak $A_{\alpha,\beta}$ is totally suppressed after 9 scans, and A_1 and A_1´ merge into a single peak, probably because of a degradation of the catalyst surface. Only the C_{oxides} and C_α peaks remain unaltered after 9 scans.

The CV responses of $Pd_{87}Cu_{13}$ follow a similar trend than those of pure Pd but with some striking differences. On the whole, C_1 (CO_2RR) is higher, $A_{\alpha,\beta}$ (H) lower (likely because of the reduced Pd content) and C_{oxides} higher, since both Cu and Pd oxides get reduced at similar potentials [33,34]. In addition, the first cycle of $Pd_{87}Cu_{13}$ exhibits the new oxidation peak A_2. It could have been assigned to CO stripping, but a close comparison between the CV response under CO_2 and Ar shows that it actually corresponds to the oxidation of copper to copper oxides/hydroxides (see references [33,34] and Figure S7 for more details about Cu corrosion and passivation in $NaHCO_3$ solutions). The absence of CO stripping peaks in the anodic domain proves that the CO produced during the cathodic scan does not remain attached to the $Pd_{87}Cu_{13}$ surface. The role of Cu in decreasing the CO adsorption energy on Pd surfaces is thus clearly evidenced at the level of the CV response.

During the second cycle, $Pd_{87}Cu_{13}$ starts behaving like pure Pd, *i.e.* $A_{\alpha,\beta}$ get suppressed, HER and C_β are considerably reduced and two CO stripping peaks appear and gradually merge (compare 8E and 8F with 8A and 8B). We assume that this Pd-like behaviour is due to the selective dissolution of Cu at the high anodic potentials attained in these experiments (*i.e.* +2.1 V *vs.* RHE, above the passivation range, as shown in Figure S7 of the SI).

Figure 9A gives the evolution of C_1 during cycling for Pd and $Pd_{87}Cu_{13}$, when the scan is restricted to the CO_2RR cathodic region. As can be seen, the CO_2RR current goes quickly to zero after 4 cycles for all samples (data from Figures 4). However, when scanning is extended to the anodic region of CO stripping (Figure 9B), *i.e.* when CO or CO-like intermediates are sequentially removed from the surface, the CO_2RR current is maintained at *c.a.* 85% of its initial value even after 10 cycles (data from Figures 8). Note that the increase of C_1 for Pd and $Pd_{87}Cu_{13}$ in the second scan is due to the recovering of H-related responses (especially C_β) after H desorption caused by the anodic scan of the first cycle.

<Figure 9>

The interest of developing a pulse method for CO_2RR on Pd-based catalysts to increase their lifetime is evident from Figure 9. However, it should be noted that Cu gets dissolved at the upper potential selected for CO stripping (+1.6 V *vs.* RHE). Anodic pulses at a potential in the foot of the CO stripping wave (*i.e.* at +1 V *vs.* RHE for Cu passivation) would be more adequate to implement such a procedure with $Pd_{100-x}Cu_x$ catalysts. Pure Pd or Pd-based alloys with more noble metals (PdPt, PdAu) are probably better candidates.

Conclusion

We have carried out an in-depth electrochemical study of the CO_2RR at $Pd_{100-x}Cu_x$ bimetallic NPs, paying special attention to the influence of the bimetallic composition on the CO_2RR response and the related CO-poisoning. Solid solution type alloys have been chosen as representative bimetallic compounds. CV and CA have been selected as electrochemical techniques, combined with a CME as a working electrode. From these experiments, the synergy between Cu and Pd, already observed by other methods (e.g. TPD-CO or XPS), has been clearly established for the first time at the level of the electrochemical responses.

The low-distorted signals provided by the CME have revealed a current plateau for $Pd_{100-x}Cu_x$ with low/intermediate Cu content (up to 50%), rather than the typical CV CO_2RR inhibition peak related to CO blocking of active Pd sites. This clearly evidences a better tolerance towards to CO poisoning for the bimetallics, as well as the transition between a CO inhibition regime for pure Pd to a diffusion-controlled regime for bimetallics. The intensity of the current plateau matches well the theoretical steady state current intensity of a microdisc (Saito's equation [35]) for a one step electron transfer. This points to a single electron transfer step as the rate limiting step CO_2RR in $Pd_{100-x}Cu_x$ alloys, as confirmed by Tafel plots.

The CA responses obtained with the CME present a particular time evolution from which three different regions can be identified: 1) double layer charging and diffusion/reaction establishment 2) beginning of the CO poisoning by formation of a CO adlayer and 3) collapse of the catalyst active sites at a critical time, t_c, closely linked with the bimetallic composition. A plot of t_c *vs.* the Pd content has a clear volcano shape, from which the composition showing the highest synergy ($Pd_{72}Cu_{28}$) and the composition from which the synergetic effect is lost ($Pd_{35}Cu_{65}$) have been clearly identified. As far as we know, this is the first time that such curve is built for Pd-based electrocatalyst (or any bimetallic electrocatalyst).

Finally, the evolution of the I/V responses with composition and time in the regions of CO_2RR and CO stripping has been thoroughly studied and the potential benefit of developing a pulse-based method to increase the lifetime of Pd-based catalysts demonstrated.

Acknowledgements

This work was financially supported by the Centre National de la Recherche Scientifique and the University Paris-Est Créteil. N.Blanchard thanks the ICMPE for his internship grant. J. Gonzalez greatly appreciates the financial support provided by the Fundacion Séneca de la Región de Murcia (Project 19887/GERM/15).

References

[1] F. Marken, D. Fermin, eds., Electrochemical Reduction of Carbon Dioxide: Overcoming the limitations of photosyntesis, RSC Energy & Enviroment Series, 2018.

[2] W. Zhang, Y. Hu, L. Ma, G. Zhu, Y. Wang, X. Xue, R. Chen, S. Yang, Z. Jin, Progress and Perspective of Electrocatalytic CO_2 Reduction for Renewable Carbonaceous

Fuels and Chemicals, Adv. Sci. 5 (2018) 1700275. https://doi.org/10.1002/advs.201700275.

[3] W. Zhu, Bimetallic Electrocatalysts for CO_2 Reduction, Topics in Current Chemistry. (2018) 21.

[4] Q. Lu, J. Rosen, F. Jiao, Nanostructured Metallic Electrocatalysts for Carbon Dioxide Reduction, ChemCatChem. 7 (2015) 38–47. https://doi.org/10.1002/cctc.201402669.

[5] T. Takashima, T. Suzuki, H. Irie, Electrochemical carbon dioxide reduction on copper-modified palladium nanoparticles synthesized by underpotential deposition, Electrochimica Acta. 229 (2017) 415–421. https://doi.org/10.1016/j.electacta.2017.01.171.

[6] F.-Y. Zhang, T. Sheng, N. Tian, L. Liu, C. Xiao, B.-A. Lu, B.-B. Xu, Z.-Y. Zhou, S.-G. Sun, Cu overlayers on tetrahexahedral Pd nanocrystals with high-index facets for CO_2 electroreduction to alcohols, Chem. Commun. 53 (2017) 8085–8088. https://doi.org/10.1039/C7CC04140C.

[7] Z. Weng, X. Zhang, Y. Wu, S. Huo, J. Jiang, W. Liu, G. He, Y. Liang, H. Wang, Self-Cleaning Catalyst Electrodes for Stabilized CO_2 Reduction to Hydrocarbons, Angewandte Chemie. 129 (2017) 13315–13319. https://doi.org/10.1002/ange.201707478.

[8] M. Li, J. Wang, P. Li, K. Chang, C. Li, T. Wang, B. Jiang, H. Zhang, H. Liu, Y. Yamauchi, N. Umezawa, J. Ye, Mesoporous palladium–copper bimetallic electrodes for selective electrocatalytic reduction of aqueous CO_2 to CO, Journal of Materials Chemistry A. 4 (2016) 4776–4782. https://doi.org/10.1039/C6TA00487C.

[9] Y. Mun, S. Lee, A. Cho, S. Kim, J.W. Han, J. Lee, Cu-Pd alloy nanoparticles as highly selective catalysts for efficient electrochemical reduction of CO_2 to CO, Applied Catalysis B: Environmental. 246 (2019) 82–88. https://doi.org/10.1016/j.apcatb.2019.01.021.

[10] Z. Yin, D. Gao, S. Yao, B. Zhao, F. Cai, L. Lin, P. Tang, P. Zhai, G. Wang, D. Ma, X. Bao, Highly selective palladium-copper bimetallic electrocatalysts for the electrochemical reduction of CO_2 to CO, Nano Energy. 27 (2016) 35–43. https://doi.org/10.1016/j.nanoen.2016.06.035.

[11] S. Ma, M. Sadakiyo, M. Heima, R. Luo, R.T. Haasch, J.I. Gold, M. Yamauchi, P.J.A. Kenis, Electroreduction of Carbon Dioxide to Hydrocarbons Using Bimetallic Cu–Pd Catalysts with Different Mixing Patterns, Journal of the American Chemical Society. 139 (2017) 47–50. https://doi.org/10.1021/jacs.6b10740.

[12] W. Zhu, L. Zhang, P. Yang, X. Chang, H. Dong, A. Li, C. Hu, Z. Huang, Z.-J. Zhao, J. Gong, Morphological and Compositional Design of Pd-Cu Bimetallic Nanocatalysts with Controllable Product Selectivity toward CO_2 Electroreduction, Small. 14 (2018) 1703314. https://doi.org/10.1002/smll.201703314.

[13] J.H. Lee, S. Kattel, Z. Jiang, Z. Xie, S. Yao, B.M. Tackett, W. Xu, N.S. Marinkovic, J.G. Chen, Tuning the activity and selectivity of electroreduction of CO 2 to synthesis gas using bimetallic catalysts, Nat Commun. 10 (2019) 1–8. https://doi.org/10.1038/s41467-019-11352-0.

[14] S. Chatterjee, C. Griego, J.L. Hart, Y. Li, M.L. Taheri, J. Keith, J.D. Snyder, Free Standing Nanoporous Palladium Alloys as CO Poisoning Tolerant Electrocatalysts for the Electrochemical Reduction of CO_2 to Formate, ACS Catal. 9 (2019) 5290–5301. https://doi.org/10.1021/acscatal.9b00330.

[15] F.V. Andrade, L.J. Deiner, H. Varela, J.F.R. de Castro, I.A. Rodrigues, F.C. Nart, Electrocatalytic Reduction of Nitrate over Palladium Nanoparticle Catalysts A Temperature-Dependent Study, J. Electrochem. Soc. 154 (2007) F159–F164. https://doi.org/10.1149/1.2752114.

[16] C. Cachet-Vivier, M. Keddam, V. Vivier, L.T. Yu, Development of cavity microelectrode devices and their uses in various research fields, Journal of Electroanalytical Chemistry. 688 (2013) 12–19. https://doi.org/10.1016/j.jelechem.2012.09.011.

[17] Lattice Parameter Determinations with an X-Ray Spectrogoniometer by the Debye-Scherrer Method and the Effect of Specimen Condition: Journal of Applied Physics: Vol 32, No 8. https://aip.scitation.org/doi/abs/10.1063/1.1728392

[18] A low-temperature X-ray diffraction study of Pd and some Pd-H alloys. Journal of Physics F: Metal Physics, Vol 8, No 1. https://iopscience.iop.org/article/10.1088/0305-4608/8/1/007

[19] L. Vegard, Die Konstitution der Mischkristalle und die Raumfüllung der Atome, Z. Physik. 5 (1921) 17–26. https://doi.org/10.1007/BF01349680.

[20] P.R. Subramanian, D.E. Laughlin, Cu-Pd (copper-palladium), Journal of Phase Equilibria. 12 (1991) 231–243.

[21] M. Allemand, Manuel.H. Martin, D. Reyter, L. Roué, D. Guay, C. Andrei, G.A. Botton, Synthesis of Cu–Pd alloy thin films by co-electrodeposition, Electrochimica Acta. 56 (2011) 7397–7403. https://doi.org/10.1016/j.electacta.2011.05.052.

[22] C. Cachet-Vivier, S. Bastide, M. Laurent, C. Zlotea, M. Latroche, Hydrogen sorption properties of Pd nanoparticles dispersed on graphitic carbon studied with a cavity microelectrode, Electrochimica Acta. 83 (2012) 133–139. https://doi.org/10.1016/j.electacta.2012.08.037.

[23] D. Plana, J. Flórez-Montaño, V. Celorrio, E. Pastor, D.J. Fermín, Tuning CO_2 electroreduction efficiency at Pd shells on Au nanocores, Chemical Communications. 49 (2013) 10962. https://doi.org/10.1039/c3cc46543h.

[24] R.-H. Guo, C.-F. Liu, T.-C. Wei, C.-C. Hu, Electrochemical behavior of CO_2 reduction on palladium nanoparticles: Dependence of adsorbed CO on electrode potential, Electrochemistry Communications. 80 (2017) 24–28. https://doi.org/10.1016/j.elecom.2017.05.005.

[25] J. Christophe, T. Doneux, C. Buess-Herman, Electroreduction of Carbon Dioxide on Copper-Based Electrodes: Activity of Copper Single Crystals and Copper–Gold Alloys, Electrocatalysis. 3 (2012) 139–146. https://doi.org/10.1007/s12678-012-0095-0.

[26] D. Gao, H. Zhou, F. Cai, D. Wang, Y. Hu, B. Jiang, W.-B. Cai, X. Chen, R. Si, F. Yang, S. Miao, J. Wang, G. Wang, X. Bao, Switchable CO_2 electroreduction via engineering active phases of Pd nanoparticles, Nano Research. 10 (2017) 2181–2191. https://doi.org/10.1007/s12274-017-1514-6.

[27] D. Gao, H. Zhou, F. Cai, D. Wang, Y. Hu, B. Jiang, W.-B. Cai, X. Chen, R. Si, F. Yang, S. Miao, J. Wang, G. Wang, X. Bao, Switchable CO_2 electroreduction via engineering active phases of Pd nanoparticles, Nano Research. 10 (2017) 2181–2191. https://doi.org/10.1007/s12274-017-1514-6.

[28] D.D. Zhu, J.L. Liu, S.Z. Qiao, Recent Advances in Inorganic Heterogeneous Electrocatalysts for Reduction of Carbon Dioxide, Adv. Mater. 28 (2016) 3423–3452. https://doi.org/10.1002/adma.201504766.

[29] K. Manthiram, B.J. Beberwyck, A.P. Alivisatos, Enhanced Electrochemical Methanation of Carbon Dioxide with a Dispersible Nanoscale Copper Catalyst, J. Am. Chem. Soc. 136 (2014) 13319–13325. https://doi.org/10.1021/ja5065284.

[30] Wiley: Electrochemical Methods: Fundamentals and Applications, 2nd Edition - Allen J. Bard, Larry R. Faulkner, 2010.

[31] C. Hou, S. Gheorghiu, V. H. Huxley, P. Pfeifer. Reverse Engineering of Oxygen Transport in the Lung: Adaptation to Changing Demands and Resources through Space-Filling Networks. https://doi.org/10.1371/journal.pcbi.1000902

[32] D. Gao, H. Zhou, J. Wang, S. Miao, F. Yang, G. Wang, J. Wang, X. Bao, Size-Dependent Electrocatalytic Reduction of CO_2 over Pd Nanoparticles, J. Am. Chem. Soc. 137 (2015) 4288–4291. https://doi.org/10.1021/jacs.5b00046.

[33] S. González, M. Pérez, M. Barrera, A.R. González Elipe, R.M. Souto, Mechanism of Copper Passivation in Aqueous Sodium Carbonate−Bicarbonate Solution Derived from Combined X-ray Photoelectron Spectroscopic and Electrochemical Data, J. Phys. Chem. B. 102 (1998) 5483–5489. https://doi.org/10.1021/jp981069k.

[34] M. Pérez Sánchez, M. Barrera, S. González, R.M. Souto, R.C. Salvarezza, A.J. Arvia, Electrochemical behaviour of copper in aqueous moderate alkaline media, containing sodium carbonate and bicarbonate, and sodium perchlorate, Electrochimica Acta. 35 (1990) 1337–1343. https://doi.org/10.1016/0013-4686(90)85004-7.

[35] Y. Saito, A Theoretical Study on the Diffusion Current at the Stationary Electrodes of Circular and Narrow Band Types, Review of Polarography. 15 (1968) 177–187. https://doi.org/10.5189/revpolarography.15.177.

Figure captions

Figure 1. Top and middle row: SEM images at 50 kX of the synthesized $Pd_{100-x}Cu_x$ nanopowders. Bottom row: magnified images (100 kX) of two compositions.

Figure 2. (A) XRD patters of $Pd_{100-x}Cu_x$ nanopowders. Top and bottom : main diffraction peaks and peak position for Cu and Pd, respectively [17,18]. (B) Lattice parameter *vs.* % at. Pd.

Figure 3. CV responses obtained with Pd NPs synthesized in this work, under (A) Argon and (B) CO_2, when the electrode is pre-treated electrochemically (solid lines) or not (dash-dotted lines). Electrolyte: $NaHCO_3$ 0.1 mol L^{-1}, v = 20 mV s^{-1} for solid lines and 5 mVs^{-1} for dash-dotted lines. The most representative electrochemical features on the curves are identified by the letters C (cathodic) or A (anodic signal) followed by a sub-index related to the process.

Figure 4. CV responses under CO_2 (red lines) and argon (black lines) obtained with the different $Pd_{100-x}Cu_x$ nanopowders. Electrolyte: $NaHCO_3$ 0. 1 mol L-1, v = 20 mV s^{-1}. Red and blue arrows show the main CO_2RR signals on Cu and Pd sites, respectively.

Figure 5. (A) Absolute value of the CO_2RR current density *vs.* at. % Pd at three potentials located in different product regions according to the literature (see Table S1). (B) CO_2RR onset potential and potential required to reach a current of 10 mA cm^{-2} *vs.* at.% Pd. Dash dotted lines are guides to the eye.

Figure 6. (A) CO_2RR current density as a function of the cycle number for a potential of -0.5 V vs. RHE. (B)-(D) CV responses of CO_2RR at Cu, Pd and $Pd_{87}Cu_{13}$ nanopowders (Figures 6B-D, respectively) for ten consecutive CV cycles, cycle number is given on the figures. Electrolyte: $NaHCO_3$ 0. 1 mol L-1, v = 20 mV s^{-1}

Figure 7. (A) Solid lines: CA responses for CO_2RR on $Pd_{100-x}Cu_x$, Pd and Cu at E = -0.4 V vs. RHE. Dash dotted line: theoretical CA response of a single one electron

transfer obtained with the Shoup-Szabo equation (Eq. S3 of the SI) with C_{CO2} = 33 mmol L^{-1}, D_{CO2}(water) = 2.1 10^{-5} cm^2 s^{-1} and r0 = 12.5 10^{-4} cm. (B) Critical time for CO poisoning vs. at. % Pd. The dash dotted line is a guide to the eye. Electrolyte: $NaHCO_3$ 0.1 mol L^{-1}.

Figure 8. CV signals for the 1st, 2nd and 9th cycle of a series of ten obtained with Pd (A, B and C) and $Pd_{87}Cu_{13}$ (D, E, F) under CO_2 (red curves) and Ar (black curves). Potential range: -1.5 to +1.5 V *vs.* Ag/AgCl (i.e. -0.9 to + 2.1 V *vs.* RHE under CO_2 and -0.8 to + 2.2 under Ar). The potential was scanned fist from E_{in} (OCP) to cathodic values (to reduce CO_2), then to anodic values (to strip CO) and back to E_{fin}.. Electrolyte: $NaHCO_3$ 0. 1 mol L^{-1}, v = 20 mV s^{-1}.

Figure 9. CO_2RR current density (at the peak C_1) vs. cycle number at Pd and $Pd_{87}Cu_{13}$ when the potential scan is restricted to the CO_2RR region and when it is extended to the region of CO stripping.

Figure 1

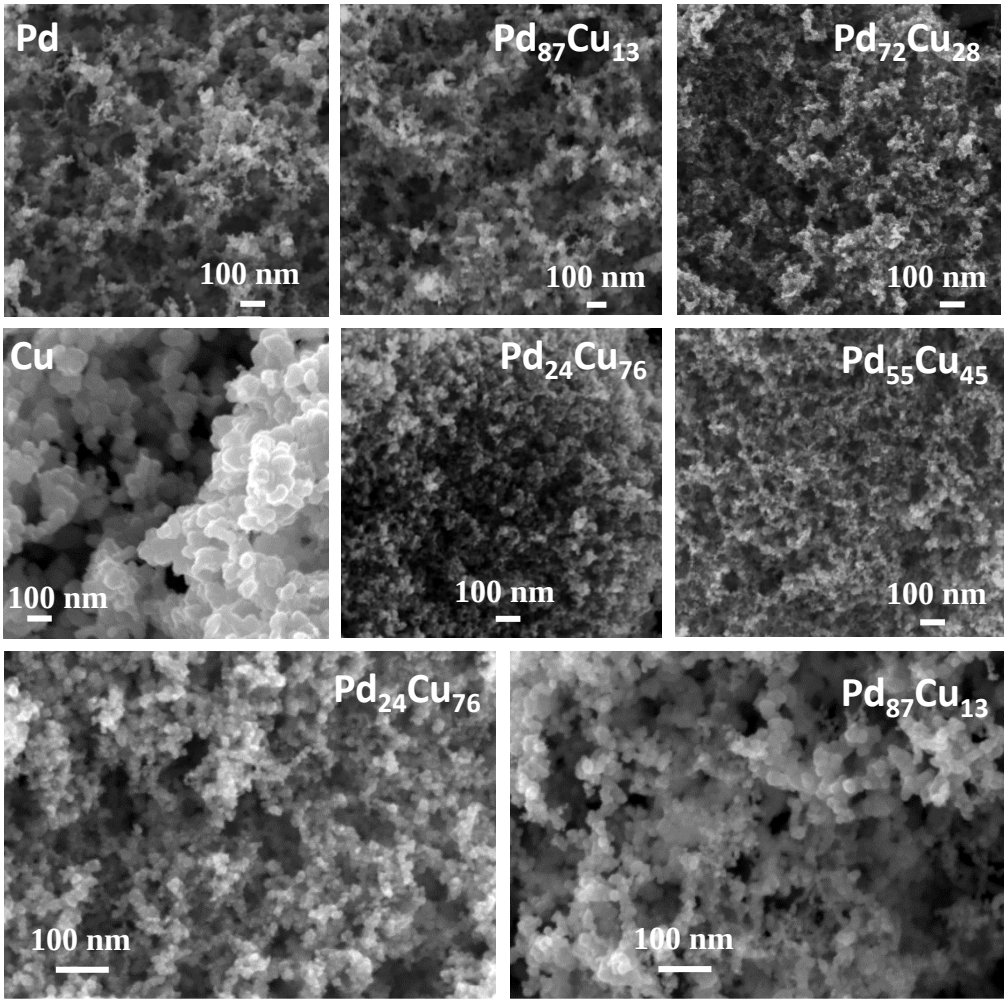
Pd
100 nm
Pd87Cu13
100 nm
Pd72Cu28
100 nm
Cu
100 nm
Pd24Cu76
100 nm
Pd55Cu45
100 nm
Pd24Cu76
100 nm
Pd87Cu13
100 nm

Figure 2

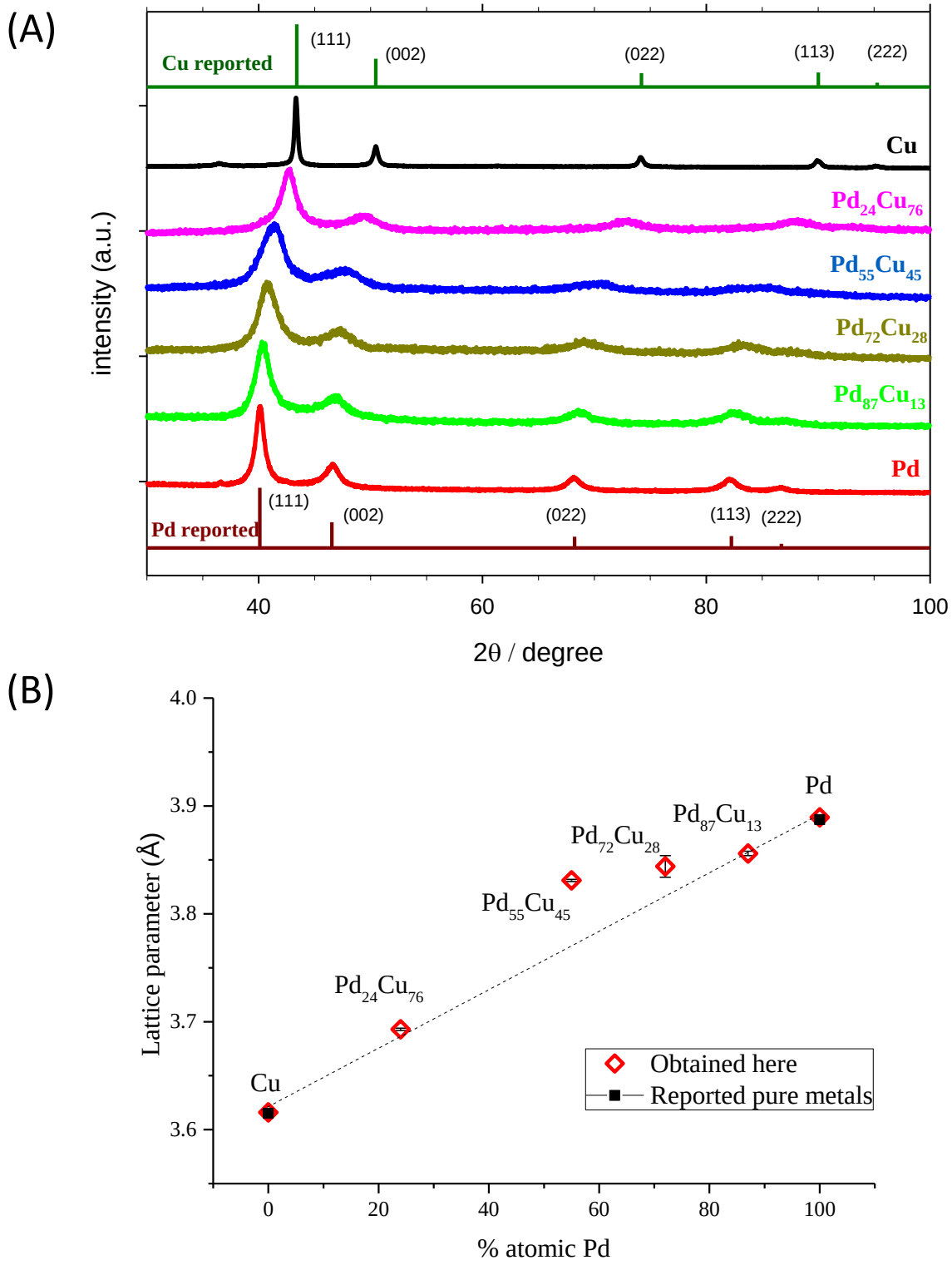
(A)
Cu reported
(111)
(002)
(022)
(113)
(222)
Cu
Pd24Cu76
Pd55Cu45
Pd72Cu28
Pd87Cu13
Pd
Pd reported
intensity (a.u.)
40
60
80
100
2θ / degree
(B)
4.0
3.9
3.8
3.7
3.6
Lattice parameter (Å)
Pd
Pd87Cu13
Pd72Cu28
Pd55Cu45
Pd24Cu76
Cu
Obtained here
Reported pure metals
0
20
40
60
80
100
% atomic Pd

Figure 3

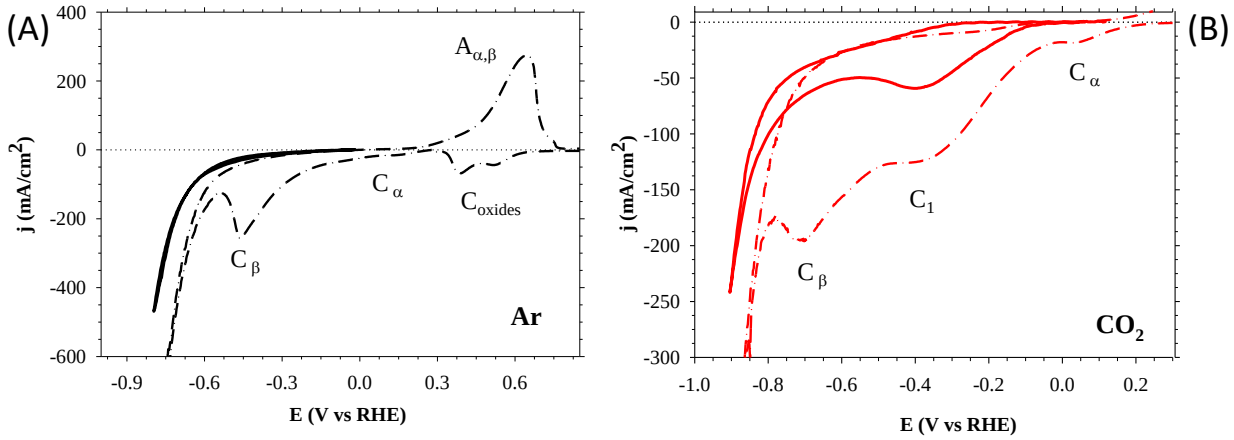
(A)
400
200
0
-200
-400
-600
j (mA/cm2)
-0.9
-0.6
-0.3
0.0
0.3
0.6
E (V vs RHE)
Aα,β
Cα
Coxides
Cβ
Ar
(B)
0
-50
-100
-150
-200
-250
-300
j (mA/cm2)
-1.0
-0.8
-0.6
-0.4
-0.2
0.0
0.2
E (V vs RHE)
Cα
C1
Cβ
CO2

Figure 4

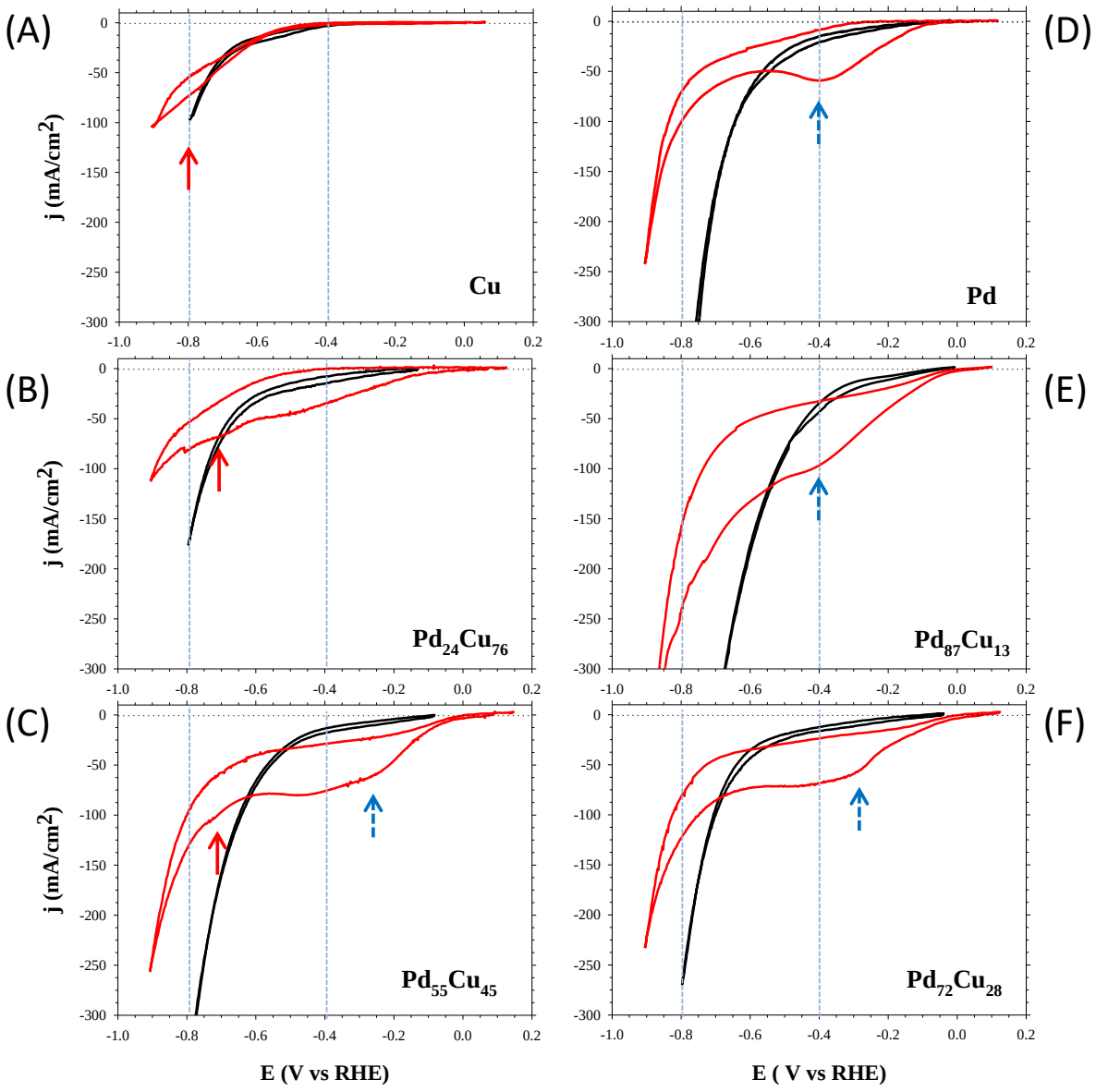
(A)
(B)
(C)
(D)
(E)
(F)
j (mA/cm2)
Cu
Pd
Pd24Cu76
Pd87Cu13
Pd55Cu45
Pd72Cu28
E (V vs RHE)
E (V vs RHE)

Figure 5

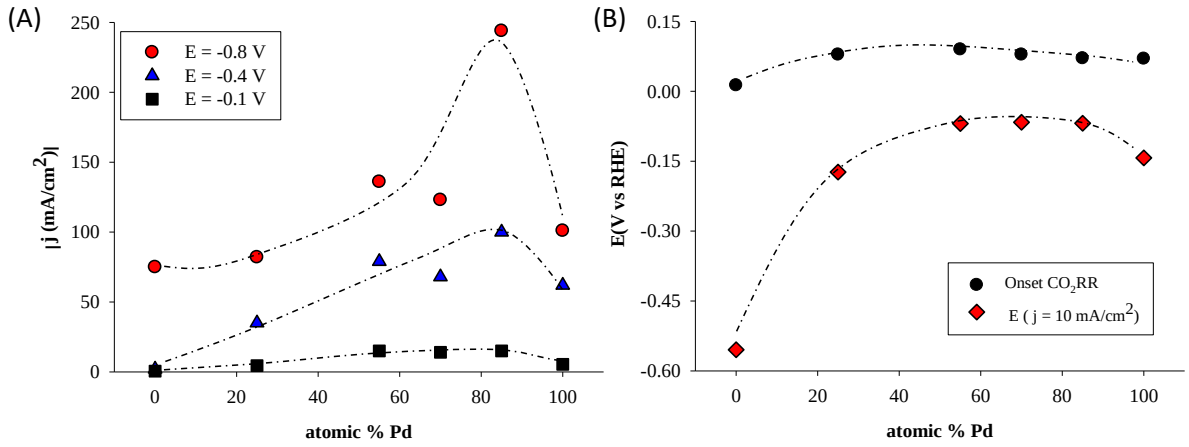

Figure 6

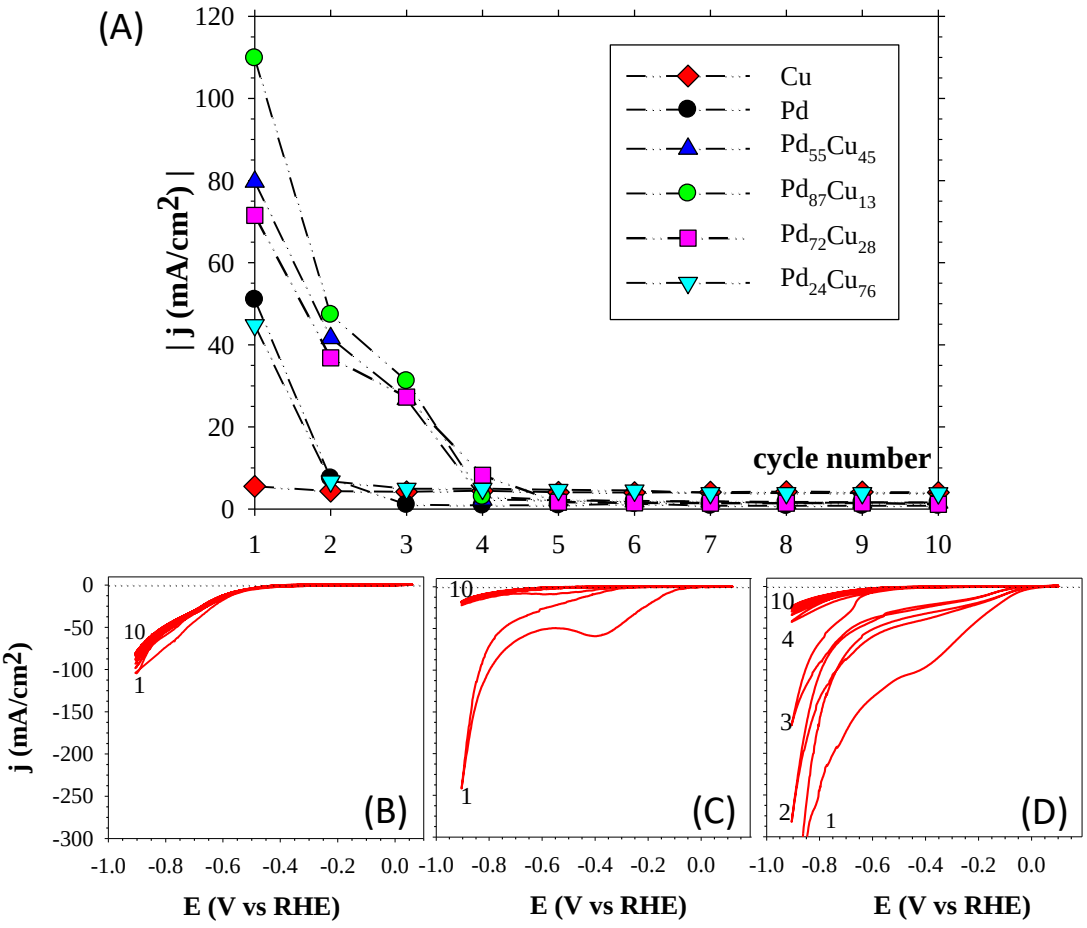

Figure 7

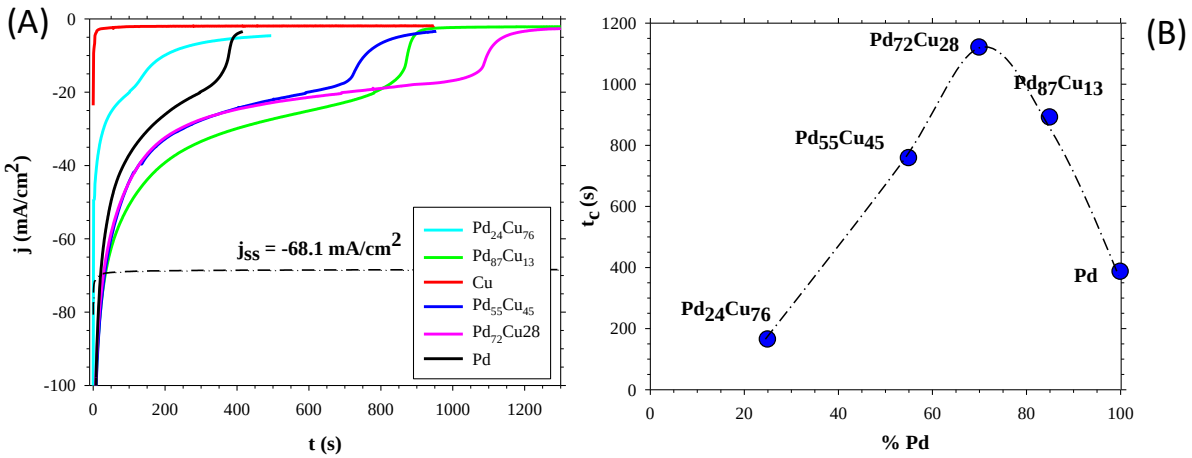
(A)
j (mA/cm2)
t (s)
jss = -68.1 mA/cm2
Pd24Cu76
Pd87Cu13
Cu
Pd55Cu45
Pd72Cu28
Pd
(B)
tC (s)
% Pd
Pd72Cu28
Pd87Cu13
Pd55Cu45
Pd
Pd24Cu76

Figure 8

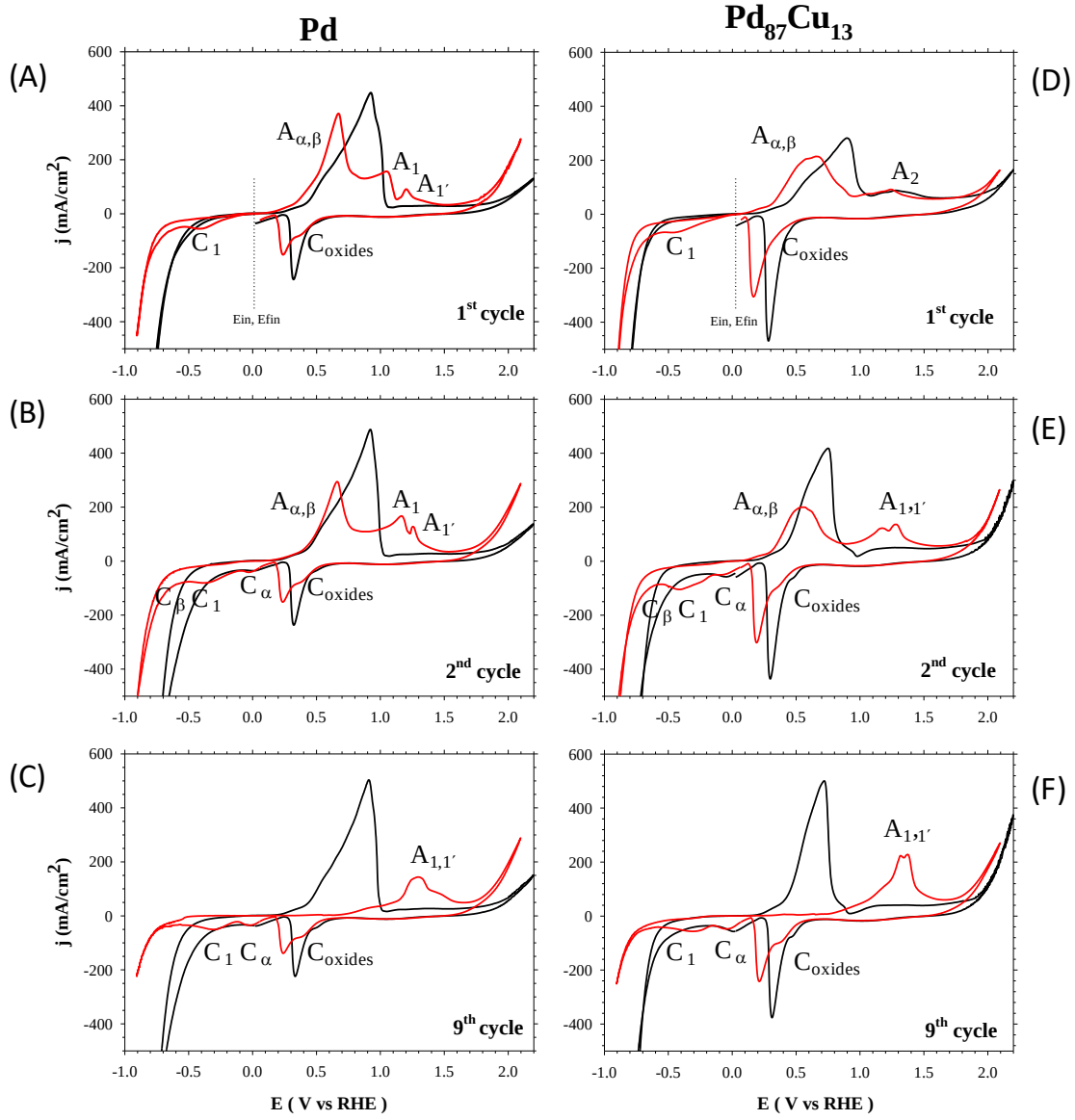
Pd
Pd87Cu13
(A)
(B)
(C)
(D)
(E)
(F)
j (mA/cm2)
E (V vs RHE)
Aα,β
A1
A1´
A2
A1,1´
C1
Cα
Cβ
Coxides
Ein, Efin
1st cycle
2nd cycle
9th cycle

Figure 9

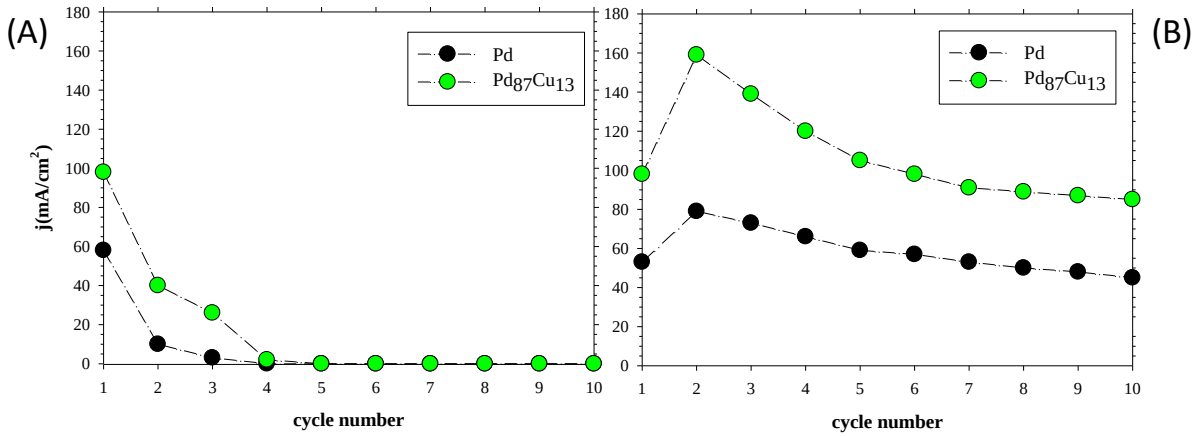

Table 1. Composition of the synthesized $Pd_{100-x}Cu_x$ nanopowders (targeted and determined by EDX), average nanoparticle size and average crystallite size.

Composition (at.%)		**Average NP size (nm)**	**Average crystallite size (nm)**
Targeted	**EDX**		
Pd	--	26 ± 2	7
$Pd_{85}Cu_{15}$	$Pd_{87}Cu_{13}$	12 ± 1	5
$Pd_{75}Cu_{25}$	$Pd_{72}Cu_{28}$	14 ± 1	5
$Pd_{50}Cu_{50}$	$Pd_{55}Cu_{45}$	11 ± 1	5
$Pd_{25}Cu_{75}$	$Pd_{24}Cu_{76}$	15 ± 2	4
Cu	--	70 ± 4	22